# A Metal−Metal Bond in the Light-Induced State of [NiFe] Hydrogenases with Relevance to Hydrogen Evolution

Mario Kampa, Maria-Eirini Pandelia,[‡] Wolfgang Lubitz, Maurice van Gastel,* and Frank Neese*

Max-Planck-Institut für Chemische Energiekonversion, Stiftstrasse 34-36, D-45470 Mülheim an der Ruhr, Germany

S *Supporting Information*

ABSTRACT: The light-induced Ni−L state of [NiFe] hydrogenases is well suited to investigate the identity of the amino acid base that functions as a proton acceptor in the hydrogen turnover cycle in this important class of enzymes. Density functional theory calculations have been performed on large models that include the complete [NiFe] center and parts of the second coordination sphere. Combined with experimental data, in particular from electron paramagnetic resonance and Fourier transform infrared (FTIR) spectroscopy, the calculations indicate that the hydride ion, which is located in the bridging position between nickel and iron in the Ni−C state, dissociates upon illumination as a proton and binds to a nearby thiolate base. Moreover, the formation of a functionally relevant nickel−iron bond upon dissociation of the hydride is unequivocally observed and is in full agreement with the observed *g* values, ligand hyperfine coupling constants, and FTIR stretching frequencies. This metal−metal bond can be protonated and thus functions like a base. The nickel−iron bond is important for all intermediates with an empty bridge in the catalytic cycle, and the electron pair that constitutes this bond thus plays a crucial role in the hydrogen evolution catalyzed by the enzyme.
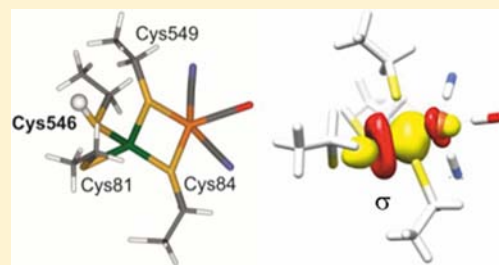
INTRODUCTION

Hydrogenases are enzymes that catalyze the reversible heterolytic splitting of molecular hydrogen. These enzymes have attracted much research interest since they are catalytically highly active (e.g., the hydrogenase from *Desulfovibrio desulfuricans* can evolve up to 9000 molecules of H_2 per second at 30 °C)[1,2] and catalyze an environmentally clean reaction. The enzymes have been studied by many physical and theoretical methods, e.g., X-ray crystallography,[3−14] Fourier transform infrared (FTIR) spectroscopy,[15−19] electron para-magnetic resonance (EPR) spectroscopy,[20−28] electrochemical methods,[29−36] extended X-ray absorption fine structure (EXAFS) and X-ray absorption (XAS) spectroscopy,[21,37−41] and quantum chemistry.[42−58] Many intermediates in the catalytic cycle have been identified, and although numerous catalytic cycles have been proposed, full consensus about the catalytic mechanism has so far not been reached.

Hydrogenases are divided into multiple classes.[59] In this contribution, the focus is on [NiFe] hydrogenases. This class carries a heterobimetallic active site, consisting of nickel and iron. The iron is in an unusual ligand environment, in which it is coordinated by one carbon-monoxide and two cyanide molecules. The two metals are bridged by two thiolates from cysteine residues. The nickel atom furthermore has two thiolate ligands that are terminally coordinated. In this configuration, the iron is five-coordinate, and nickel is four-coordinate.[3−14] A third bridging position may be occupied by different molecules in the intermediates of the catalytic cycle.[15,43,48] The nickel atom is believed to be the center of activity for hydrogen

evolution.[60] The enzymes also harbor three accessory iron−sulfur clusters functioning as an electron relay.[3−14]

Three intermediate states have been identified, that are believed to be part of the catalytic cycle.[15,61] These states are commonly referred to as Ni−Si$_a$ ("nickel-silent-active"), Ni−C, and Ni−R. These species have been characterized by a unique fingerprint of stretching frequencies of the CO and CN ligands. The oxidation state of iron is formally 2+ and low spin in all intermediate states, since the diatomic ligands give rise to a large crystal field splitting. The oxidation state of nickel is formally 2+ in the case of Ni−Si$_a$ and Ni−R[15] and 3+ in the case of Ni−C.[21−23] The Ni−R state is two-electrons more reduced than Ni−Si$_a$, and the Ni−C state is one-electron more reduced with respect to Ni−Si$_a$.[15,19] Electron nuclear double resonance (ENDOR) and hyperfine sublevel correlation (HYSCORE) spectroscopy have confirmed the presence of a bridging hydride in the Ni−C state,[20−22,24,62] which is believed to be originating from the heterolytic splitting of H_2. In a recent extended study of the Ni−C state by density functional theory (DFT), which included the [NiFe] center and the second coordination sphere, the hydride was confirmed to be bound to both nickel and iron, with the iron being in an octahedral and the nickel being in a square pyramidal ligand field.[55]

Illumination of the Ni−C state at temperatures <200 K leads to conversion to the Ni−L state. The formation of the Ni−L state was discovered for the first time in the [NiFe] hydrogenase from *Allochromatium vinosum*[63] and was later

found to also occur in other [NiFe] hydrogenases.[64,65] The action spectrum associated with the conversion from Ni−C to Ni−L was found to contain a maximum at 590 nm.[66] By EPR[66] and HYSCORE[22,24] experiments,[22,66] it could be shown that the signal assigned to the bridging hydride in the Ni−C state disappears in the course of the photoconversion. This has prompted the suggestion, corroborated by DFT calculations by Hall et al,[67] that the hydride ligand is removed from the bridging position in the form of a proton, which then binds to a nearby basic amino acid or water molecule. In fact, multiple Ni−L states have been observed by EPR spectroscopy, indicating that the proton can be taken up by more than one nearby base.[21,63,65] Although the Ni−L state is not believed to be functionally relevant (e.g., hydrogenases function equally well in the dark), the light-induced Ni−L state is well suited to investigate the identity of an amino acid base that may function as a proton acceptor in the catalytic cycle. In addition, the Ni−L state also serves as a paramagnetic model for the investigation of the electronic structure of reaction intermediates with an empty bridging position. Further evidence for photodissociation and reassociation of the hydride ligand is available from rapid scan kinetic measurements,[68] by which it was demonstrated that binding of the proton to the nearby base is a first-order process. The kinetics of the back-conversion into the Ni−C state was studied in H_2O and D_2O buffer, and the primary kinetic isotope effect was found to lie between 5 and 7.[68] In addition, the light-induced formation of Ni−L was studied with FTIR spectroscopy by monitoring the changes of the stretching frequencies of the iron-bound CO and CN ligands.[69−71]

Formally, conversion of the hydride into a proton proceeds under concomitant two-electron reduction of the nickel atom from 3+ to 1+. However, Ni L-edge XAS experiments[41] are in contrast to this assignment and predict a three-valent nickel similar to Ni−C. Single crystal EPR on the Ni−L state of the *Desulfovibrio vulgaris* Miyazaki F hydrogenase by Förster et al[23] furthermore revealed that the orientations of the **g**-tensor axes of Ni−L are almost equal to those in Ni−C. With $g_z = 2.05$, $g_y = 2.12$ and $g_x = 2.30$, the **g**-tensor components differ from those obtained for Ni−C, but the smallest g value remains associated with the z direction. The most notable difference concerns the g_z value, which in Ni−C equals 2.01 and is close to the free electron g-value, g_e, while for Ni−L a significantly larger value is found (2.05).[22,24] In the study by Förster et al.,[23] the interpretation of the experimental results was corroborated by DFT calculations using a Ni−L cluster model including the first coordination shell. The experimental findings were most compatible with **g**-tensor calculations considering a formal monovalent nickel center and a vacant bridging position. Analysis of the electronic structure revealed that the singly occupied orbital exhibits mainly nickel d_{z^2} character, as is the case for the Ni−C state, with smaller contributions of the nickel $d_{x^2−y^2}$ orbital. However, since the $d_{x^2−y^2}$ orbital is the lowest unoccupied orbital in the Ni−C state, concomitant two-electron reduction of the nickel center upon Ni−L formation, would lead to a singly occupied $d_{x^2−y^2}$ orbital rather than a singly occupied d_{z^2} orbital. This would result in a **g** tensor with the largest instead of the smallest g value pointing along the z direction. This, however, is incompatible with experiment.[61]

It is thus still an open question, to which basic amino acid in the vicinity of the [NiFe] core the photodissociated proton binds. Also, the oxidation state of nickel is still under debate, information which is relevant for the catalytic cycle of the enzyme. In this study, we address these questions by extended DFT calculations using large models of the [NiFe] center that include the second coordination sphere. Computed **g** tensors, hyperfine coupling tensors, and stretching frequencies of the CN and CO ligands have been compared to experimental data and indeed shed light on the geometric and electronic structure of the Ni−L state.

■ MATERIALS AND METHODS

Ni−L Model Geometries. Cluster models for the Ni−L state have been derived from the HisHε model, which has recently been shown to provide an accurate description of the geometric and electronic structure of the Ni−C state.[55] The HisHε model has been constructed from the X-ray structure of the reduced *D. vulgaris* Miyazaki F hydrogenase (pdb: 1H2R).[7] A thorough description of the HisHε model is given in ref 55. In summary, the model consists of the two metal atoms, the bridging hydride, the two CN⁻, and one CO ligands bound to Fe and the four nickel-coordinating cysteines modeled as ethylthiolates. The amino acid residues Glu34, Val83, His88, Asp123, Pro476, Ala477, Arg479, Leu482, Val500, Pro501, and Ser502 are included as well. The amino acids have been truncated at a distance larger than 4 Å from the $[NiFeS_4(CO)(CN)_2]$ core, whereby functional groups, e.g., carboxyl groups have been retained. The added hydrogen atoms and the atoms to which they are bound have been constrained in the geometry optimization. The *D. vulgaris* Miyazaki F numbering of amino acids is used consistently throughout this manuscript.

Similarly, the Ni−L cluster model contains the [NiFe] core, which consists of nickel, iron, the four nickel-coordinating cysteine residues modeled as ethylthiolates, the CN and CO ligands to iron, and amino acid fragments of the second coordination sphere as specified before.[55] The hydride ligand has been removed from the bridging position in the Ni−L cluster models, and one cysteine sulfur atom has been protonated. For the terminal cysteines Cys81 and Cys546, two orientations of the proton are possible, and hence, two models (A, B) have been considered for each cysteine. Thus, six cluster models have been constructed, denoted as H^+81-A, H^+81-B, H^+84, H^+546-A, H^+546-B, and H^+549. The structures of the first coordination shell of these models are presented in Figure 1. In addition, a seventh model designated as 'deprot' has been considered, in which the proton has not been included (not shown).

Computational Details. The Ni−L cluster models contain 164 atoms and 1424 contracted basis functions (Table 1). All cluster models are spin $S = 1/2$ systems. The total charge of the cluster models is 2−, while it is 3− for the deprot model. All calculations have been performed with the ORCA program package.[72] Geometry optimizations and IR spectra have been calculated with the BP86 GGA functional[73,74] due to its well-documented good performance in these areas.[75,76] In contrast to the HisHε model for the Ni−C state, the spin contamination of the wave function is significant when the hybrid functional B3LYP is used. With spin contaminations of almost 0.4, this holds especially true for H^+84 and H^+549. In contrast, since Hartree−Fock exchange is absent in the BP86 functional, the spin contamination for the BP86 functional is negligible. Accordingly, not only geometry optimizations and IR spectra but also magnetic properties and energies calculations have been performed with the BP86 functional.

The def2-TZVP (geometries) and def2-TZVP(-f) basis set[77] (properties) has been chosen for Ni and Fe and the complete first coordination sphere, which includes all cysteine sulfur atoms, the two CN and one CO ligands. For all other atoms, the def2-SV(P) basis sets has been employed for geometry optimization and the def2-SVP for the calculation of spectroscopic properties. The RI approximation[78] has been applied in conjunction with a def2-SVP auxiliary basis set. Scalar relativistic effects have been taken in account in the form of the ZORA approximation[79,80] in conjunction with scalar relativistic recontractions of the def2-basis sets.[77] The COSMO model[81] with a dielectric constant of $\varepsilon = 4$ and Grimme's 2006 van der Waals correction[82] have been employed in property calculations and the
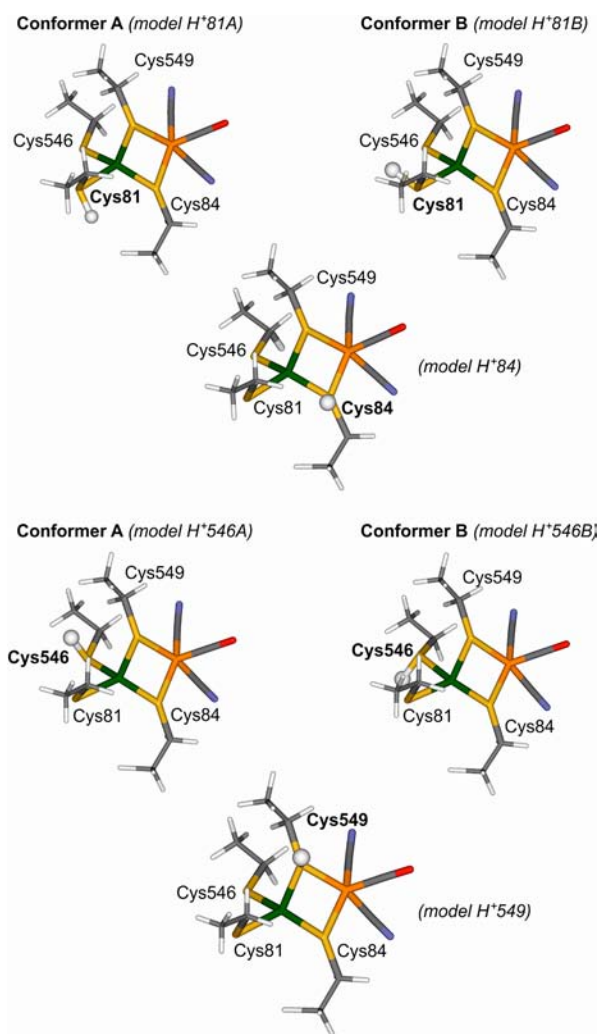
Figure 1. Cluster models for the Ni−L state. The models feature an unoccupied bridging position and one protonated cysteine residue. Two orientations of the proton are possible for protonation at Cys546 and Cys81. The corresponding model clusters are called H⁺546-A, H⁺546-B, H⁺81-A, and H⁺81-B. Not shown is the deprot model in which the photodissociated proton has not been included. Color coding: nickel (green), iron (orange), sulfur (yellow), carbon (gray), nitrogen (blue), oxygen (red), and hydrogen (white).

geometry optimizations. The COSMO model has not been used for vibrational frequency calculations.

■ RESULTS

Geometries. A crystal structure for the Ni−L state has not been reported so far. Geometries are therefore only shortly discussed. In Table 2, selected geometric parameters of the geometry-optimized Ni−L models and the HisHε model are collected. The Ni−S distances show no systematic variation

within the different Ni−L cluster models. Exceptions are the H⁺84 and the H⁺549 cluster models, in which a bridging thiolate is protonated. For these models, the distance between metal and protonated bridging sulfur atom becomes shorter.

The Ni−Fe distance of the other models is slightly larger than that found for HisHε. Interestingly, the range of Hβ(1)(Cys546)-Cβ(Cys546)-Sγ(Cys546)-Ni torsion angles in the various Ni−L models with values of −29.6° to −49.5° indicates a certain degree of flexibility of the terminal ligand Cys546. The torsion angle βH(1)(Cys549)-βC(Cys549)-γS-(Cys549)-Ni varies less strongly among the multiple Ni−L models than the corresponding angle for Cys546, presumably due to the stabilizing hydrogen bond between Sγ(Cys549) and H(ε) of His88. The exact conformations of the cysteine residues Cys546 and Cys549 are likely even affected by the more distant parts of the protein framework. Inclusion of these interactions, which is beyond the scope of this work, can in principle be realized by performing QM/MM calculations. For hydrogenase, such studies have already been carried out by Söderhjelm[83] and Jayapal,[84] albeit for the Ni−SI and Ni−R states. One result of these QM/MM studies is that torsion angles still display a method-related dependence on the employed functional of typically 5°, and we therefore prefer not to interpret the exact value of the torsion angles or their spread any further.

Electronic Structure. Upon illumination of the Ni−C state, the hydride leaves the bridging position as a proton and may bind to one of the cysteines. This would correspond to a formal two-electron reduction of the d^7 Ni^{3+} to a d^9 Ni^{1+} center. In the Ni−C state the d_{z^2} orbital is singly occupied, whereas the $d_{x^2-y^2}$ orbital is unoccupied. Hence, two-electron reduction of the nickel center would concomitantly lead to a doubly occupied d_{z^2} orbital and a singly occupied $d_{x^2-y^2}$ orbital with significantly different g values and ligand hyperfine interactions. Since the spin−orbit coupling matrix element of $d_{x^2-y^2}$ and d_{xy} would give rise to a dominant contribution to second order to the g_z value (e.g., in many Cu(II) complexes with a singly occupied $d_{x^2-y^2}$ orbital the g_z value attains values typically between 2.2 and 2.3),[85] one would expect the largest g-tensor component in the z-direction. This, however, is not observed experimentally.[23] In addition, XAS experiments have not confirmed the presence of a reduced nickel center but rather indicate an oxidation state similar to that in Ni−C.[41] Therefore, the available experimental data do not appear consistent with the presence of the unpaired electron in the $d_{x^2-y^2}$ orbital, indicative of a d^9 Ni^{1+} species. The question thus arises: Where do the two electrons of the former hydride go upon photodissociation?

In Figure 2, the orbital diagram is presented for the frontier orbitals of the Ni−C and Ni−L states. The diagram has been restricted to only the $d_{x^2-y^2}$ and d_{z^2} orbitals, since consideration of these orbitals will suffices for understanding the changes in electronic structure upon photodissociation of Ni−C to form

Table 1. Number of Atoms and Contracted Basis Functions, Total Charge, and Spin Contaminations

	H⁺81-A	H⁺81-B	H⁺84	H⁺546-A	H⁺546-B	H⁺549	HisHε	deprot
atoms	165	165	165	165	165	165	165	164
basis functions	1424	1424	1424	1424	1424	1424	1424	1418
charge	2−	2−	2−	2−	2−	2−	2−	3−
<S2> BP	0.77	0.77	0.77	0.77	0.77	0.77	0.76	0.78
<S2> B3LYP	0.86	0.88	1.14	0.88	0.87	1.12	0.77	1.15

Table 2. Selected Bond Distances [Å] and Torsion Angles Ω_{546} (Hβ(1)(Cys546)-Cβ(Cys546)-Sγ(Cys546)-Ni) and Ω_{549} (Hβ(1)(Cys549)-Cβ(Cys549)-Sγ(Cys549)-Ni) [°] from the Geometry-Optimized Ni−L Cluster Models

	H⁺81-A	H⁺81-B	H⁺84	H⁺546-A	H⁺546-B	H⁺549	HisHε
Ni−S(Cys81)	2.31	2.28	2.30	2.32	2.33	2.31	2.25
Ni−S(Cys84)	2.25	2.26	2.17	2.22	2.22	2.26	2.27
Ni−S(Cys546)	2.17	2.17	2.14	2.21	2.21	2.17	2.18
Ni−S(Cys549)	2.28	2.27	2.28	2.26	2.28	2.19	2.34
Fe−S(Cys84)	2.29	2.29	2.19	2.28	2.28	2.29	2.3
Fe−S(Cys549)	2.29	2.29	2.29	2.28	2.28	2.22	2.31
Ni−Fe	2.56	2.56	2.66	2.58	2.58	2.64	2.54
Ω_{546}	−29.6	−34.0	−35.0	−30.4	−49.5	−33.5	−43.2
Ω_{549}	1.2	0.4	−2.5	−2.3	−4.3	−6.3	−1.3
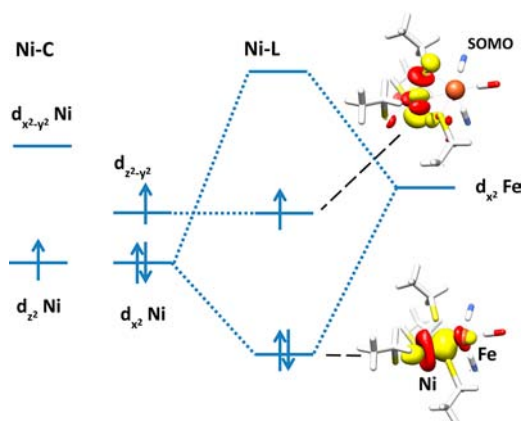
Figure 2. Frontier orbital diagram for the Ni−C (leftmost levels only) and Ni−L states. The insets show orbitals for Ni−L, which have been obtained from a quasirestricted wave function in the H⁺Cys546-A model. The doubly occupied orbital corresponding to the Ni−Fe bond has been obtained by localization.[99]

Ni−L (*vide infra*). The **g**-tensor principal axes system has been chosen as the coordinate system.[23] In this axis system the *z*-direction points along the Ni−Sγ(Cys549) bond and the Ni−Sγ(Cys81) direction is located in the *xz* plane. A stereoview picture including the axis system is given in the Supporting Information (SI). Since the hydride ligand is removed from the equatorial plane, the $d_{x^2-y^2}$ orbital is lowered in energy relative to the one in Ni−C. In order to interpret the bonding interactions of nickel for Ni−L, it turns out to be practical to consider the d_{x^2} and $d_{z^2-y^2}$ orbitals, which can be formed by a linear combination of the d_{z^2} and the $d_{x^2-y^2}$ orbitals:

$$d_{x^2} = -\frac{1}{2}d_{z^2} + \frac{\sqrt{3}}{2}d_{x^2-y^2} \tag{1a}$$

$$d_{z^2-y^2} = -\frac{\sqrt{3}}{2}d_{z^2} + \frac{1}{2}d_{x^2-y^2} \tag{1b}$$

The lobes of the d_{x^2} orbital point approximately along the Ni−Sγ(Cys81) bond and toward the vacant bridging position. The lack of a hydride ligand opens the possibility to form a bent metal−metal σ interaction by bonding and antibonding combinations of the nickel d_{x^2} orbital and the iron d_{x^2} orbital (both orbitals are of course not perfectly aligned along the *x* axis). The C_∞ symmetry axis of each orbital forms a small angle with respect to the *x* axis, but we retain this nomenclature in order to prevent overly complicated labeling of the involved orbitals). The DFT calculation reveals that the corresponding localized Ni−Fe orbital is centered by 81% at nickel and by

15% at iron (see inset of Figure 2). The antibonding combination of the nickel d_{x^2} orbital and the iron d_{x^2} orbital is unoccupied, while the singly occupied molecular orbital has $d_{z^2-y^2}$ character (see inset of Figure 2). The energy difference between the bonding and antibonding orbitals, calculated from a CAS calculation and with the side note that two spin couplings are possible to attain a spin-adapted doublet state with three unpaired electrons, amounts to about 29 000 and 34 000 cm⁻¹, respectively. The dominant contribution of the nickel $d_{z^2-y^2}$ orbital to the singly occupied orbital is corroborated by the Mulliken spin populations presented in Table 3. Significant mixing of the d_{z^2} and $d_{x^2-y^2}$ orbitals is

Table 3. Mulliken Spin Populations of the Nickel d_{z^2} and $d_{x^2-y^2}$ Orbitals

	d_{z^2}	$d_{x^2-y^2}$
H⁺81-A	0.25	0.16
H⁺81-B	0.39	0.19
H⁺84	0.37	0.16
H⁺546-A	0.43	0.14
H⁺546-B	0.40	0.14
H⁺549	0.43	0.12

observed, with the d_{z^2} orbital being the main contribution. The coordination of a hydride to both nickel and iron in the Ni−C state can thus be viewed of as a protonation of the electron pair that forms the nickel−iron bond. In Ni−C, the electron pair is counted to the hydride and a metal−metal bond is formally absent, whereas upon photodissociation to Ni−L, the base becomes deprotonated and the electron pair formally forms a nickel−iron bond. Hence, back-conversion of Ni−L to the Ni−C state can be interpreted as protonation of the bound bimetallic center of the hydrogenase active site. Mayer bond orders (cf. Table 4) corroborate the formation of a nickel−iron bond in the Ni−L state with bond orders of about 0.4 for all models. This is larger by 0.1 than the corresponding value for the HisHε model. However, despite the finding of a Ni−Fe bond order of ~0.3 for the HisHε model, the interaction of the two metals and the hydride in Ni−C is best described as Ni−H−Fe three-center bond, whereas in the case of Ni−L, a genuine two-center metal−metal bond is present. Possibly, the formation of Ni−L occurs only due to the stabilization of the active site by this Ni−Fe bond, which partially compensates for the loss of the favorable interactions of the hydride with the two metals. The bond order for the S−H bond formed by the protonated sulfur atom of one of the cysteines and the former hydride is 0.9 for the terminal cysteines and 0.8 for the bridging cysteines indicating a normal covalent sulfur−hydrogen bond.

Table 4. Mayer Bond Orders of Selected Bonds

	H$^+$81-A	H$^+$81-B	H$^+$84	H$^+$546-A	H$^+$546-B	H$^+$549	deprot	HisHε
Ni−S(81)	0.50	0.48	0.60	0.60	0.60	0.61	0.52	0.75
Ni−S(84)	0.70	0.68	0.71	0.74	0.74	0.68	0.69	0.70
Ni−S(546)	0.99	0.98	1.04	0.70	0.68	1.04	0.85	1.04
Ni−S(549)	0.62	0.63	0.63	0.67	0.65	0.66	0.63	0.60
Fe−S(81)	0.69	0.68	0.67	0.68	0.68	0.72	0.58	0.64
Fe−S(546)	0.60	0.62	0.61	0.61	0.62	0.64	0.90	0.60
S−H	0.89	0.90	0.82	0.92	0.92	0.81	−	−
Fe−H	−	−	−	−	−	−	−	0.39
Ni−H	−	−	−	−	−	−	−	0.51
Ni−Fe	0.37	0.38	0.38	0.38	0.38	0.37	0.40	0.29

Table 5. Mulliken Charges^a

	H$^+$81-A	H$^+$81-B	H$^+$84	H$^+$546-A	H$^+$546-B	H$^+$549	deprot	Ni−C
S(81)	−0.14	−0.18	−0.43	−0.48	−0.51	−0.41	−0.48	−0.37
S(84)	−0.21	−0.23	0.04	−0.18	−0.19	−0.16	−0.19	−0.10
S(546)	−0.30	−0.35	−0.21	−0.03	−0.03	−0.21	−0.35	−0.20
S(549)	−0.22	−0.24	−0.21	−0.18	−0.21	0.03	−0.22	−0.15
Ni	−0.15	−0.13	−0.11	−0.11	−0.11	−0.11	−0.04	−0.24
Fe	0.09	0.10	0.03	0.10	0.11	0.00	0.11	−0.10
H$^+$	0.09	0.11	0.09	0.12	0.11	0.08	−	0.25

^{a}H$^+$ designates the photodissociated proton.

Since electron density is shared with the proton, formation of a covalent S−H bond results in a smaller absolute Mulliken charge of the sulfur atom in question, i.e., the sulfur becomes more charge neutral. The Mulliken charge for the remaining sulfur atoms becomes more negative compared to the HisHε model. For the Ni−L models, the Mulliken charge at the nickel atom is similar to the one in the HisHε model. The finding of a formal charge of 3+ instead of 1+ in L-edge XAS experiments for the Ni−L state[41] can be rationalized by this transfer of electron density from the nickel center to the sulfur ligands and, in addition, to the iron center via the metal−metal bond. On a side note, the extreme difference between the formal charge of 3+ at nickel and the actual Mulliken charge of about −0.1 is an indication that the formal charge is only useful for bookkeeping purposes when counting the number of electrons.

The spin population at the nickel atom, ranging from 0.6 to 0.7, is larger than in the HisHε model with a value of 0.5. Concomitantly, spin delocalization is reduced, and the sulfur atom of Cys549 exhibits a Mulliken spin population between 0.17 and 0.22, whereas the spin population at this sulfur atom is 0.3 in the HisHε model. For the H$^+$549 model the spin population even decreases to a value of 0.1. The spin population of the sulfur atom of Cys546, on the other hand, increases relative to the HisHε model, except, of course, when the residue itself is protonated (Table 5).

Spin density plots for the H$^+$549, H$^+$546-A, H$^+$84 and H$^+$81-B models are displayed in Figure 3. The plots for H$^+$546-B and H$^+$81-A are similar to those for H$^+$546-A and H$^+$81-B, respectively, and are therefore not shown. In agreement with the orbital diagram (Figure 2), the contours of the spin density at the nickel center indicate that the relevant orbital at nickel is best classified as a $d_{z^2-y^2}$ orbital. Significant amounts of spin density are found in the 3p orbitals of Sγ(Cys549) and Sγ(Cys546). For H$^+$546-A, the spin density at Sγ(Cys546) almost vanishes, in agreement with the Mulliken spin populations in Table 6. Close inspection of the spin density plot for H$^+$546-A reveals that the singly occupied orbital at
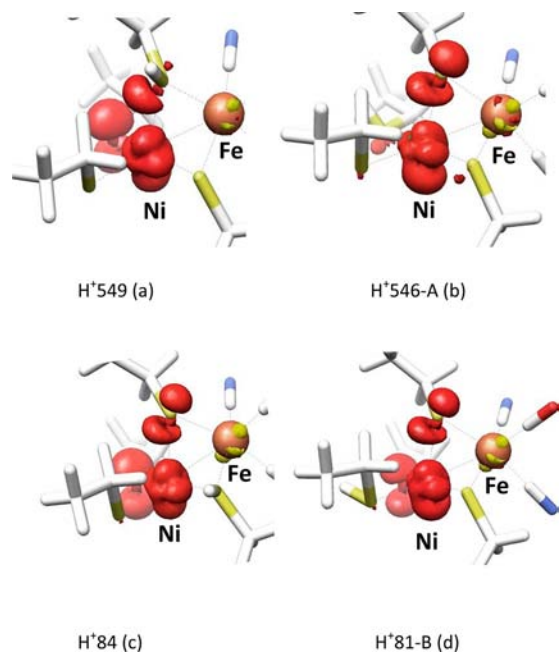

Figure 3. Spin density plots for the Ni−L models (a) H$^+$549, (b) H$^+$546-A, (c) H$^+$84, and (d) H$^+$81-B.

Sγ(Cys549) is not a pure 3p orbital but also contains s-orbital contributions. In contrast to second-row elements, like carbon, the 3s and 3p valence orbitals of sulfur are energetically more separated and s−p mixing occurs to a smaller degree. However, for protonation and thereby formation of a fourth bond, the sulfur 3p orbitals of Cys549 mix with the 3s orbital, i.e., the 3p orbitals become hybridized, which is also reflected by changes in the sulfur bond angles. For example, the Ni−Sγ(Cys549)-Fe bond angle increases from 66° to 74°, which is accommodated by an elongation of the Ni−Fe distance and a contraction of the Sγ(Cys549)-Fe and Sγ(Cys549)-Ni bonds. The same reasoning holds for the sulfur atom of Cys84 in the H$^+$Cys84 model.

Table 6. Mulliken Spin Populations[a]

	H$^+$81-A	H$^+$81-B	H$^+$84	H$^+$546-A	H$^+$546-B	H$^+$549	deprot	Ni−C
S(81)	0.01	0.01	0.02	0.04	0.03	0.01	0.02	0.00
S(84)	0.04	0.04	0.04	0.05	0.05	0.02	0.05	0.00
S(546)	0.19	0.17	0.26	0.05	0.03	0.23	0.13	0.15
S(549)	0.18	0.19	0.17	0.22	0.22	0.11	0.18	0.29
Ni	0.63	0.65	0.59	0.68	0.70	0.63	0.71	0.51
Fe	−0.07	−0.08	−0.09	−0.06	−0.05	−0.03	−0.10	0.02
H$^+$	0.00	0.00	−0.01	0.00	0.00	0.00	−0.01	0.00

[a]H$^+$ designates the photodissociated proton.

In summary, the electronic structure of the Ni−L models differs markedly from that of the HisHε model for the Ni−C state. In the Ni−C state the metal contribution to the singly occupied molecular orbital is the nickel d_{z^2} orbital with its C_∞ axis pointing approximately along the Ni−Sγ(Cys549) bond. In the Ni−L state, a bond is formed between nickel and iron. Rehybridization of the nickel d-orbitals occurs, such that the d_{x^2} orbital pointing in the direction of the unoccupied bridging position forms a metal−metal bond with the iron d_{x^2} orbital. Thus, the interaction of the nickel and iron centers in Ni−L is different from that in Ni−C where a three-center two-electron bond is present, formed by the Fe d_{x^2}, the Ni $d_{x^2-y^2}$, and the hydride s-orbital. As opposed to the Ni−C state, the singly occupied molecular orbital in Ni−L is not a d_{z^2} orbital but a $d_{z^2-y^2}$ orbital, which results in significantly altered magnetic properties, in particular **g** tensors (*vide infra*). In addition, the Mulliken spin populations at the sulfur atoms of Cys549 and Cys546 are smaller and larger, respectively, as compared to the values for Ni−C and, hence, also ^{1}H hyperfine tensors of the β-CH$_2$ groups of Cys549 and Cys546 are different from those of Ni−C (*vide infra*).

Energies. Energies for the conversion from Ni−C to Ni−L are collected in Table 7. All energies are positive which means

Table 7. Energies ΔE [kcal/mol] for the Conversion From Ni−C to Ni−L

	ΔE
H$^+$81-A	17
H$^+$81-B	15
H$^+$84	26
H$^+$546-A	8
H$^+$546-B	20
H$^+$549	27

that the conversion from Ni−L back to Ni−C is energetically favorable for all cluster models. The Ni−L models H$^+$549 and H$^+$84 have the highest energies, and hence, protonation at a bridging cysteine is energetically more costly than protonation of the terminal cysteines. The two conformers H$^+$81-A and H$^+$81-B exhibit almost equal energies. On the other hand, the conversion energy for H$^+$546-B is larger by more than 10 kcal/mol than that of H$^+$546-A. With only 8 kcal/mol, the latter model features the lowest energy for Ni−L formation among the Ni−L models.

The conversion energies exhibited by all Ni−L cluster models are positive in agreement with the experimental finding that the Ni−L state is only accessible by a photochemical reaction but not a thermal reaction. Furthermore, the energies are in line with the finding that the Ni−L state readily converts back to the Ni−C state above an enzyme-dependent annealing

temperature. Apparently, at lower temperatures, the enzyme is kinetically trapped. Due to their similar energy, the two conformers H$^+$81-A and H$^+$81-B would possibly occur in a thermal equilibrium. The prevalence of one of the two structures would be possible only if one conformer is formed exclusively upon illumination and the conversion into the other conformer is sufficiently slowed down by a large energy barrier. Similarly, observation of H$^+$546-B is only possible if a sufficiently large energy barrier prevents its conversion into the energetically more stable conformation H$^+$546-A.

Since the potential energy surface of the excited state on which the photochemical formation of Ni−L takes place is not known, it cannot be determined by consideration of the energy alone which of the cysteines likely becomes protonated. Hence, in order to come to a structural assignment of the Ni−L state and to see whether protonation of the cysteine residue is compatible with the observed g values and hyperfine couplings, a comparison of computed and experimental spectroscopic data is indispensable and is considered next.

EPR Spectroscopy of Ni−L. Calculated and experimental g values are summarized in Table 8. As evident from the table,

Table 8. Computed g Values for Models of Ni−L and Ni−C (HisHε) and Experimental g Values

	g$_z$	g$_y$	g$_x$	g$_{iso}$
H$^+$81-A	2.04	2.05	2.11	2.07
H$^+$81-B	2.04	2.05	2.12	2.07
H$^+$84	2.04	2.06	2.09	2.06
H$^+$546-A	2.04	2.06	2.12	2.07
H$^+$546-B	2.04	2.06	2.12	2.07
H$^+$549	2.04	2.08	2.12	2.08
deprot	2.05	2.07	2.12	2.08
HisHε	2.01	2.07	2.10	2.06
exp Ni−C[23]	2.01	2.14	2.20	2.12
exp Ni−L[23]	2.05	2.12	2.30	2.15

the computed g values for the multiple cluster models accurately reproduce the experimentally observed difference between the g$_z$ values of Ni−C and Ni−L. As is well-known from reference calculations, the largest g shift for various metals, including Cu(II) and Ni(I)/Ni(III), is usually underestimated by up to 30%.[86] Indeed, the same is found here—the calculated g$_x$ values are systematically smaller than the experimental ones. This systematic underestimation has been attributed partly to an overestimated spin delocalization into ligand orbitals.[86] Compared to the hybrid B3LYP functional, the spin delocalization is even stronger for the BP86 used here due to the lack of Hartree−Fock exchange. Therefore, the underestimation of the **g** tensor relative to experiment is very pronounced. Experimentally, a smaller g$_y$ and a larger g$_x$

component have been observed in the Ni−L state with respect to Ni−C. This trend is reproduced at least qualitatively except for the H⁺549 and H⁺84 models, where bridging thiolates are protonated. Thus, within the given accuracy of the calculated g values, cluster models H⁺81-A, H⁺81-B, H⁺546-A and H⁺546-B are most compatible with experiment.

Fortunately, not only the g values but also the directions of the principal axes are experimentally known. In Table 9, the

Table 9. Orientations of the Principal Axes of the Calculated and Experimental g Tensors

axis	g_z	g_y	g_x	g_z	g_y	g_x
	H⁺81-A			H⁺81-B		
a	−0.94	0.11	0.33	−0.81	0.45	0.37
b	−0.23	−0.90	−0.36	−0.57	−0.72	−0.39
c	−0.26	0.42	−0.87	−0.09	0.53	−0.84
	H⁺84			H⁺546-A		
a	−0.71	0.49	0.51	−0.77	0.13	0.63
b	−0.67	−0.70	−0.26	−0.45	−0.81	−0.38
c	−0.23	0.53	−0.82	−0.46	0.57	−0.68
	H⁺546-B			H⁺549		
a	−0.86	0.05	0.51	−0.82	0.54	0.19
b	−0.30	−0.85	−0.43	−0.57	−0.80	−0.20
c	−0.42	0.52	−0.74	−0.04	0.28	−0.96
	deprot			HisHε		
a	−0.79	0.47	0.40	−0.79	0.37	0.48
b	−0.60	−0.73	−0.32	−0.55	−0.77	−0.32
c	−0.14	0.49	−0.86	−0.26	0.52	−0.81
	exp Ni−C[23]			exp Ni−L[23]		
a	−0.76	0.46	0.46	−0.75	0.36	0.56
b	−0.59	−0.78	−0.20	−0.59	−0.74	−0.33
c	−0.27	0.43	−0.86	−0.30	0.57	−0.77

orientations of the principal axes of the **g** tensor are summarized. Experimentally, the orientations of the **g**-tensor axes of Ni−L were found to be similar to those of the Ni−C state with the **g**$_z$ axis pointing approximately along the Ni−Sγ(Cys549) bond, **g**$_y$ along Ni−Sγ(Cys546), and **g**$_x$ along Ni−Sγ(Cys81). Indeed, the orientations of the **g**-tensor are suitably reproduced by all models. Upon comparison of the calculated directions with the experimental ones for Ni−L, best agreement is reached with H⁺546-A and H⁺546-B models and worst agreement with H⁺549. Though the orientations of the **g**$_z$ and **g**$_y$ components are less accurately reproduced, it has to be noted that because of the near axiality of the calculated **g** tensor the direction cosines have little meaning (cf. Table 8).

In the framework of second-order perturbation theory, all spin−orbit coupling matrix elements in the z direction vanish for the Ni−C state, and the **g**$_z$ component equals the free electron g value. In contrast, in the Ni−L state, a positive contribution to **g**$_z$ comes from an excited state, which arises from the transition of an electron from the d$_{xy}$ orbital into the d$_{z^2-y^2}$ singly occupied orbital. Since **g**$_z$ is the smallest g value, it can be deduced that d$_{xy}$ is lower in energy than d$_{xz}$ and d$_{yz}$. Contributions to **g**$_y$ and **g**$_x$ arise from matrix elements between the d$_{z^2-y^2}$ orbital and the d$_{xz}$ and d$_{yz}$ orbitals, respectively. For the Ni−C state the d$_{yz}$ orbital is found higher in energy than the d$_{xz}$ orbital resulting in a **g** tensor with **g**$_x$ > **g**$_y$. The removal of the hydride ligand, which in the Ni−C state lies along the x-axis, stabilizes the d$_{xz}$ orbital. Consequently, also in the Ni−L state, d$_{xz}$ should be found at a lower energy with respect to d$_{yz}$ which results in a **g** tensor with **g**$_x$ > **g**$_y$ and essentially

unchanged principal axes, which is indeed found both experimentally and computationally. Also, the angular momentum matrix elements of d$_{yz}$ with the d$_{z^2-y^2}$ singly occupied orbital for Ni−L is larger by a factor of $2/\sqrt{3}$ than the matrix element of d$_{yz}$ with the d$_{z^2}$ orbital for Ni−C. The larger matrix element is in agreement with the fact that the **g**$_x$ component is larger in the Ni−L state with respect to that in the Ni−C state.

In summary, the **g** tensor orientations of Ni−L are the same as those of the Ni−C state. However, the g values for the Ni−L state differ significantly from those for Ni−C. The most prominent deviation is found for the **g**$_z$ component, which for Ni−L (2.05) differs significantly from the free electron g value (g_e). This can be attributed to the existence of the nonvanishing matrix element of the d$_{z^2-y^2}$ orbital with the d$_{xy}$ orbital in the Ni−L state. Furthermore, the **g**$_x$ component is larger than that for Ni−C. The g values and directions of the principal axes are best reproduced by the H⁺546-B model.

The ¹H hyperfine coupling constants of the two protons of the $β$-CH$_2$ group of Cys549 are presented in Table 10. The

Table 10. ¹H hyperfine Coupling Constants [MHz] of the Two Protons of the $β$CH$_2$ Group of Cys549

	A_1	A_2	A_3	A_{iso}
	H(1)			
H⁺81-A	8	10	15	11
H⁺81-B	8	10	15	11
H⁺84	6	8	13	9
H⁺546-A	12	13	18	14
H⁺546-B	11	13	17	14
H⁺549	0	2	7	3
deprot	9	11	16	12
HisHε	13	16	20	16
exp Ni−C[24]	11	12	18	14
	H(2)			
H⁺81-A	5	6	9	7
H⁺81-B	5	6	9	7
H⁺84	4	5	8	6
H⁺546-A	7	7	11	8
H⁺546-B	8	9	12	10
H⁺549	6	7	9	7
deprot	6	7	10	7
HisHε	10	11	15	12
exp Ni−C[24]	10	11	15	12

magnitude of the ¹H isotropic hyperfine couplings is largely determined by the spin density at the sulfur atom of Cys549. For the HisHε model, the isotropic hyperfine couplings in Table 10 are larger compared to those obtained for Ni−C with the B3LYP functional.[55] This is in line with the finding of a larger spin population at the sulfur atom of Cys549 (Table 6) compared to the corresponding values obtained with B3LYP. The computed isotropic hyperfine coupling for H(1) in the HisHε model for Ni−C is slightly larger than the experimentally observed value, but the value for H(2) is in accurate agreement with the experimental one. In the Ni−L models, the isotropic hyperfine coupling constants of H(1) range between 9 and 14 MHz, with H⁺546-A and H⁺546-B yielding the largest values. An exception is clearly the H⁺549 model with a hyperfine coupling of only 3 MHz, which is in agreement with the observed reduction of the spin density at the sulfur atom of Cys549 upon protonation relative to HisHε. Therefore, the isotropic hyperfine coupling constants of the

Ni−L models are smaller than the corresponding ones obtained with HisHε. For H(2) the Ni−L models yield isotropic hyperfine coupling constants which range from 6 to 10 MHz. They are all smaller than the corresponding values for H(1), with the exception of the H+549 model.

Computed ^{1}H hyperfine coupling constants for the H(1) and H(2) protons of the β-CH$_2$ group of Cys546 are presented in Table 11. The coupling constants for the cluster models

Table 11. [1]H hyperfine Coupling Constants [MHz] of the Two Protons of the βCH$_2$ Group of Cys546

	A_1	A_2	A_3	A_{iso}
	H(1)			
H+81-A	15	15	19	16
H+81-B	11	11	15	13
H+84	19	20	24	21
H+546-A	−1	−1	3	0
H+546-B	−1	−2	2	0
H+549	19	19	23	21
deprot	11	12	15	13
HisHε	10	11	14	12
exp Ni−C[24]	7.3	7.3	12	8.9
	H(2)			
H+81-A	13	14	18	15
H+81-B	13	14	18	15
H+84	18	19	24	20
H+546-A	2	3	7	4
H+546-B	0	0	4	1
H+549	14	15	20	16
deprot	8	9	13	10
HisHε	13	14	18	15

H+546-A and H+546-B are small, which is in line with the relatively small Mulliken spin population at Sγ(Cys546) found for these models (Table 11). The hyperfine tensors of the other Ni−L models are dominated by the isotropic contributions, which are comparable or larger in magnitude than the corresponding ones for the HisHε model. In particular, H+549 and H+84 exhibit fairly large isotropic values up to 21 MHz. The 'deprot' model gives an isotropic coupling for H(2), which is smaller by 5 MHz than the corresponding value for HisHε, while the value of H(1) is similar to that found in the HisHε model. These differences are relatively small and result from a slight reorientation of the Cys546 residue, as described in the Geometries section.

In the Supporting Information, ^{1}H ENDOR spectra of the oxygen tolerant regulatory hydrogenase (RH) from the aerobic bacterium *Ralstonia eutropha*, recorded with a modified Davis-ENDOR sequence, are displayed. In this enzyme, two Ni−L states have been observed with slightly different g values.[22] These states have been denoted by the labels Ni−L (or Ni−L1) and Ni−L$_A$ (or Ni−L2). The spectroscopic properties of the active site of RH are otherwise almost identical to those of oxygen-sensitive hydrogenases.[24] In *R. eutropha*, by raising the temperature for 20 min to 200 K, the Ni−L state converts to the Ni−L2 state. Upon further increase of the temperature, the enzyme converts back to Ni−C. Inspection of the ENDOR spectra immediately reveals that the signals with largest hyperfine shifts in Ni−C, assigned to the β-CH$_2$ protons of Cys549, have smaller hyperfine shifts in Ni−L1 and Ni−L2. Thus, the ENDOR spectra also indicate that the spin density at Cys549 is significantly reduced in both Ni−L states as

compared to Ni−C. Given that the anisotropy of these signals, as measured by orientation-selected ENDOR spectra, is similar in Ni−L and Ni−C, the ENDOR spectra also confirm that the directions of principal axes of the **g** tensor as well as the orientation of the Cys549 residue is identical in Ni−C and Ni−L.

Upon photoconversion of the Ni−C state to the Ni−L state, the signal corresponding to the bridging hydride disappears.[21,22,24] A proton bound to one of the thiolates is expected to have smaller ^{1}H hyperfine coupling constants than the hydride. The computed ^{1}H hyperfine coupling constants of the thiolate-bound proton are presented in Table 12. The isotropic

Table 12. Computed [1]H Hyperfine Couplings [MHz] of the Photodissociated Proton

	A_1	A_2	A_3	A_{iso}
H+81-A	0	−7	−7	−5
H+81-B	2	−5	−5	−3
H+84	−6	−12	−13	−10
H+546-A	3	4	11	6
H+546-B	8	9	11	9
H+549	17	21	26	21
exp Ni−L2	2.6	−4.8	−4.3	−2.2

hyperfine coupling constant in the H+81-A, H+81-B and H+84 models is negative, whereas it is positive in the H+546-A, H+546-B and H+549 models. The largest absolute values are found for H+84 and H+549 with the latter amounting to even more than 20 MHz, which is clearly incompatible with the ENDOR experiment. The values in the models with protonated terminal thiolates are much smaller and would give rise to signals with hyperfine shifts between 0 and 5.5 MHz, which correlates well with the ENDOR experiments. In order to experimentally verify the presence of a protonated thiolate, additional pulsed ENDOR experiments have been performed on the Ni−L2 state of the regulatory hydrogenase of *R. eutropha*. This enzyme has been shown to display Ni−C and Ni−L states with essentially identical spectroscopic properties as the one from *D. vulgaris* Miyazaki F.[24] A ^{2}H ENDOR spectrum, obtained by reducing the enzyme with D$_2$ in a deuterated solvent, is given in the Supporting Information. The hyperfine coupling constants deduced from the spectra are included in Table 12 and agree well with the H+81 models, in particular H+81-B.

IR Spectroscopy. Stretching frequencies of the CO and CN ligands bound to the iron center are collected in Table 13. Since the CO stretching frequencies are systematically underestimated in DFT calculations of metal−carbonyl compounds, a constant shift of 28 cm^{-1} has been proposed to correct the calculated frequencies.[87,88] The experimentally found CO stretching frequency for Ni−L is 50 cm^{-1} smaller than that for Ni−C. All Ni−L cluster models yield a CO stretching frequency smaller than that for HisHε, by ∼30 cm^{-1}. The CO frequencies for the models H+81-A, H+81-B, H+546-A, and H+546-B are almost equal and are about 15 cm^{-1} larger than the experimental Ni−L value. The H+84 model yields a value that is even 30 cm^{-1} larger than the experimental one. On the other hand, the value for the 'deprot' model is almost 15 cm^{-1} smaller compared to experiment.

The two experimentally determined CN modes exhibit smaller stretching frequencies compared to those found for Ni−C, which is also reproduced by the Ni−L cluster models

3922

dx.doi.org/10.1021/ja3115899 | *J. Am. Chem. Soc.* 2013, 135, 3915−3925

Table 13. IR Stretching Frequencies $[\text{cm}^{-1}]$ of the CO and CN Ligands Bound to the Fe Atom[a]

	CO	CN	CN
H^+81-A	1925	2032	2055
H^+81-B	1925	2033	2055
H^+84	1940	2047	2067
H^+546-A	1924	2031	2052
H^+546-B	1923	2031	2053
H^+549	1924	2049	2065
deprot	1896	2006	2031
HisHε	1957	2062	2083
exp Ni−C[19]	1961	2074	2085
exp Ni−L[68]	1911	2048	2061

[a]The CO frequencies have been adjusted by an additive systematic correction of $+28$ cm^{-1}.[87,88]

with protonated terminal thiolates. The computed values for the Ni−C state using the HisHε model are in good agreement with experiment for the higher-frequency antisymmetric stretching mode but underestimate the lower-frequency symmetric mode by about 12 cm^{-1}. The CN frequency shifts from Ni−C to Ni−L are again best reproduced by the H^+81-A, H^+81-B, H^+546-A, and H^+546-B models, in which a terminal thiolate becomes protonated.

CONCLUSION

In this work, we have performed a systematic quantum chemical study for the Ni−L state of [NiFe] hydrogenases. The Ni−L state arises from the Ni−C state by illumination which results in the photodissociation of the bridging hydride and formal reduction to a monovalent oxidation state. The photodissociated proton is expected to bind to a basic residue in the vicinity of the active site, since upon raising the temperature, the Ni−L state is readily converted back to the Ni−C state.

Multiple models have been used, which feature a vacant bridging position. The photodissociated proton has been attached to one of the cysteines or left out of the model completely. The electronic structure of the Ni−L state differs markedly from that of the Ni−C state. The LUMO $d_{x^2-y^2}$ and the SOMO d_{z^2} orbital of Ni−C rehybridize into a $d_{z^2-y^2}$ and d_{x^2} orbital in the Ni−L state. The SOMO is mainly composed of the $d_{z^2-y^2}$ orbital, which results in a **g** tensor with different $\mathbf{g}_x$ and $\mathbf{g}_z$ values as compared to the Ni−C state. The C_∞ orbital axis of the doubly occupied d_{x^2} orbital points in the direction of the unoccupied bridging position and forms a metal−metal bond with the d_{x^2} orbital of the Fe center. Such a metal−metal interaction has recently been also observed in model systems that are catalytically active toward hydrogen production.[89−91] Formally, upon photoconversion of Ni−C to Ni−L, the nickel center adopts a d^9 Ni^{1+} electron configuration. However, the Mulliken charge population of the nickel is even slightly more positive with respect to Ni−C, which is accommodated by the accumulation of significant amounts of additional negative charge at the cysteines. This is in agreement with XAS measurements predicting a Ni^{3+} instead of a Ni^{1+} oxidation state. In this respect, the nickel and iron atoms can be viewed as a base with the Ni−Fe bond being the electron pair, which is protonated for Ni−C and unprotonated for Ni−L. The formation of the Ni−Fe bond is presumably essential for the occurrence of the Ni−L state at low temperatures, as it partly compensates for the loss of the stabilizing interactions of the

hydride with the two metals. The formation of a metal−metal bond is not only relevant for the stabilization of the Ni−L state but is likely also important for intermediates in the catalytic cycle, which also feature a vacant bridging site. Vice versa, the nickel−iron bond can be protonated and in case of the Ni−C state serves as a base for one of the substrate hydrogen atoms. Calculated spectroscopic parameters, i.e., **g** tensors, hyperfine couplings and IR-frequencies, all agree with the presence of the metal−metal bond between nickel and iron.

Concerning the identity of the base that binds the proton upon photodissociation of the hydride, the models with protonated terminal thiolates (H^+546-A, H^+546-B, H^+81-A, and H^+81-B) match the experimental findings best. In particular, quantitative agreement for the Ni−L2 state is obtained with the cluster model H^+81-B. Since, according to our investigation, the terminal cysteines act as basic residues which become protonated in the Ni−L state, it is conceivable that these residues also act as nucleophiles for hydrogen abstraction in the course of the catalytic mechanism. This is in agreement with the conclusions drawn from various experimental and computational studies[10,11,15,56,92−98] of the reaction mechanism of [NiFe] hydrogenases.

ASSOCIATED CONTENT

Ⓢ Supporting Information

A stereoview picture including the axis system. ^{1}H ENDOR spectra of the oxygen tolerant regulatory hydrogenase (RH) from the aerobic bacterium *Ralstonia eutropha*. ^{2}H ENDOR spectrum, obtained by reducing the enzyme with D_2 in a deuterated solvent. This material is available free of charge via the Internet at http://pubs.acs.org.

AUTHOR INFORMATION

Corresponding Author

frank.neese@cec.mpg.de; maurice.van-gastel@cec.mpg.de

Present Address

‡Department of Chemistry, Pennsylvania State University, State College, Pennsylvania 16802, United States.

Notes

The authors declare no competing financial interest.

ACKNOWLEDGMENTS

REFERENCES

(1) Cammack, R. *Nature* **1999**, *397*, 214.
(2) Hatchikian, E. C.; Forget, N.; Fernandez, V. M.; Williams, R.; Cammack, R. *Eur. J. Biochem.* **1992**, *209*, 357.
(3) Volbeda, A.; Charon, M. H.; Piras, C.; Hatchikian, E. C.; Frey, M.; Fontecilla-Camps, J. C. *Nature* **1995**, *373*, 580.
(4) Volbeda, A.; Garcin, E.; Piras, C.; de Lacey, A. L.; Fernandez, V. M.; Hatchikian, E. C.; Frey, M.; Fontecilla-Camps, J. C. *J. Am. Chem. Soc.* **1996**, *118*, 12989.
(5) Higuchi, Y.; Yagi, T.; Yasuoka, N. *Structure* **1997**, *5*, 1671.
(6) Montet, Y.; Amara, P.; Volbeda, A.; Vernede, X.; Hatchikian, E. C.; Field, M. J.; Frey, M.; Fontecilla-Camps, J. C. *Nat. Struct. Biol.* **1997**, *4*, 523.
(7) Higuchi, Y.; Ogata, H.; Miki, K.; Yasuoka, N.; Yagi, T. *Struct. Fold. Des.* **1999**, *7*, 549.

(8) Nicolet, Y.; Piras, C.; Legrand, P.; Hatchikian, C. E.; Fontecilla-Camps, J. C. *Struct. Fold. Des.* **1999**, *7*, 13.

(9) Nicolet, Y.; de Lacey, A. L.; Vernede, X.; Fernandez, V. M.; Hatchikian, E. C.; Fontecilla-Camps, J. C. *J. Am. Chem. Soc.* **2001**, *123*, 1596.

(10) Ogata, H.; Mizoguchi, Y.; Mizuno, N.; Miki, K.; Adachi, S.; Yasuoka, N.; Yagi, T.; Yamauchi, O.; Hirota, S.; Higuchi, Y. *J. Am. Chem. Soc.* **2002**, *124*, 11628.

(11) Volbeda, A.; Montet, Y.; Vernede, X.; Hatchikian, E. C.; Fontecilla-Camps, J. C. *Int. J. Hydrogen Energy* **2002**, *27*, 1449.

(12) Volbeda, A.; Martin, L.; Cavazza, C.; Matho, M.; Faber, B. W.; Roseboom, W.; Albracht, S. P. J.; Garcin, E.; Rousset, M.; Fontecilla-Camps, J. C. *J. Biol. Inorg. Chem.* **2005**, *10*, 239.

(13) Ogata, H.; Hirota, S.; Nakahara, A.; Komori, H.; Shibata, N.; Kato, T.; Kano, K.; Higuchi, Y. *Structure* **2005**, *13*, 1635.

(14) Ogata, H.; Kellers, P.; Lubitz, W. *J. Mol. Biol.* **2010**, *402*, 428.

(15) Bleijlevens, B.; Faber, B. W.; Albracht, S. P. J. *J. Biol. Inorg. Chem.* **2001**, *6*, 763.

(16) de Lacey, A. L.; Hatchikian, E. C.; Volbeda, A.; Frey, M.; Fontecilla-Camps, J. C.; Fernandez, V. M. *J. Am. Chem. Soc.* **1997**, *119*, 7181.

(17) George, S. J.; Kurkin, S.; Thorneley, R. N. F.; Albracht, S. P. J. *Biochemistry* **2004**, *43*, 6808.

(18) Kurkin, S.; George, S. J.; Thorneley, R. N. F.; Albracht, S. P. J. *Biochemistry* **2004**, *43*, 6820.

(19) Fichtner, C.; Laurich, C.; Bothe, E.; Lubitz, W. *Biochemistry* **2006**, *45*, 9706.

(20) Fan, C. L.; Teixeira, M.; Moura, J.; Moura, I.; Huynh, B. H.; Legall, J.; Peck, H. D.; Hoffman, B. M. *J. Am. Chem. Soc.* **1991**, *113*, 20.

(21) Whitehead, J. P.; Gurbiel, R. J.; Bagyinka, C.; Hoffman, B. M.; Maroney, M. J. *J. Am. Chem. Soc.* **1993**, *115*, 5629.

(22) Brecht, M.; van Gastel, M.; Buhrke, T.; Friedrich, B.; Lubitz, W. *J. Am. Chem. Soc.* **2003**, *125*, 13075.

(23) Foerster, S.; Stein, M.; Brecht, M.; Ogata, H.; Higuchi, Y.; Lubitz, W. *J. Am. Chem. Soc.* **2003**, *125*, 83.

(24) Foerster, S.; van Gastel, M.; Brecht, M.; Lubitz, W. *J. Biol. Inorg. Chem.* **2005**, *10*, 51.

(25) van Gastel, M.; Stein, M.; Brecht, M.; Schröder, O.; Lendzian, F.; Bittl, R.; Ogata, H.; Higuchi, Y.; Lubitz, W. *J. Biol. Inorg. Chem.* **2006**, *11*, 41.

(26) Carepo, M.; Tierney, D. L.; Brondino, C. D.; Yang, T. C.; Pamplona, A.; Telser, J.; Moura, I.; Moura, J. J. G.; Hoffman, B. M. *J. Am. Chem. Soc.* **2002**, *124*, 281.

(27) Goenka-Agrawal, A.; van Gastel, M.; Gärtner, W.; Lubitz, W. *J. Phys. Chem. B* **2006**, *110*, 8142.

(28) Flores, M.; Goenka-Agrawal, A.; van Gastel, M.; Gärtner, W.; Lubitz, W. *J. Am. Chem. Soc.* **2008**, *130*, 2402.

(29) Pershad, H. R.; Duff, J. L. C.; Heering, H. A.; Duin, E. C.; Albracht, S. P. J.; Armstrong, F. A. *Biochemistry* **1999**, *38*, 8992.

(30) Jones, A. K.; Sillery, E.; Albracht, S. P. J.; Armstrong, F. A. *Chem. Commun.* **2002**, 866.

(31) Leger, C.; Jones, A. K.; Albracht, S. P. J.; Armstrong, F. A. *J. Phys. Chem. B* **2002**, *106*, 13058.

(32) Leger, C.; Jones, A. K.; Roseboom, W.; Albracht, S. P. J.; Armstrong, F. A. *Biochemistry* **2002**, *41*, 15736.

(33) Jones, A. K.; Lamle, S. E.; Pershad, H. R.; Vincent, K. A.; Albracht, S. P. J.; Armstrong, F. A. *J. Am. Chem. Soc.* **2003**, *125*, 8505.

(34) Lamle, S. E.; Albracht, S. P. J.; Armstrong, F. A. *J. Am. Chem. Soc.* **2004**, *126*, 14899.

(35) Vincent, K. A.; Cracknell, J. A.; Lenz, O.; Zebger, I.; Friedrich, B.; Armstrong, F. A. *Proc. Natl. Acad. Sci. U.S.A.* **2005**, *102*, 16951.

(36) Vincent, K. A.; Parkin, A.; Lenz, O.; Albracht, S. P. J.; Fontecilla-Camps, J. C.; Cammack, R.; Friedrich, B.; Armstrong, F. A. *J. Am. Chem. Soc.* **2005**, *127*, 18179.

(37) Maroney, M. J.; Colpas, G. J.; Bagyinka, C.; Baidya, N.; Mascharak, P. K. *J. Am. Chem. Soc.* **1991**, *113*, 3962.

(38) Whitehead, J. P.; Colpas, G. J.; Bagyinka, C.; Maroney, M. J. *J. Am. Chem. Soc.* **1991**, *113*, 6288.

(39) Bagyinka, C.; Whitehead, J. P.; Maroney, M. J. *J. Am. Chem. Soc.* **1993**, *115*, 3576.

(40) Gu, Z. J.; Dong, J.; Allan, C. B.; Choudhury, S. B.; Franco, R.; Moura, J. J. G.; LeGall, J.; Przybyla, A. E.; Roseboom, W.; Albracht, S. P. J.; Axley, M. J.; Scott, R. A.; Maroney, M. J. *J. Am. Chem. Soc.* **1996**, *118*, 11155.

(41) Davidson, G.; Choudhury, S. B.; Gu, Z. J.; Bose, K.; Roseboom, W.; Albracht, S. P. J.; Maroney, M. J. *Biochemistry* **2000**, *39*, 7468.

(42) Pavlov, M.; Siegbahn, P. E. M.; Blomberg, M. R. A.; Crabtree, R. H. *J. Am. Chem. Soc.* **1998**, *120*, 548.

(43) Siegbahn, P. E. M.; Blomberg, M. R. A.; Pavlov, M. W. N.; Crabtree, R. H. *J. Biol. Inorg. Chem.* **2001**, *6*, 460.

(44) Siegbahn, P. E. M. *C. R. Acad. Sci., Ser. IIc: Chim.* **2007**, *10*, 766.

(45) Siegbahn, P. E. M.; Tye, J. W.; Hall, M. B. *Chem. Rev.* **2007**, *107*, 4414.

(46) Lill, S. O. N.; Siegbahn, P. E. M. *Biochemistry* **2009**, *48*, 1056.

(47) Stein, M.; Lubitz, W. *J. Inorg. Biochem.* **2001**, *86*, 442.

(48) Stein, M.; Lubitz, W. *Phys. Chem. Chem. Phys.* **2001**, *3*, 2668.

(49) Stein, M.; Lubitz, W. *Curr. Opin. Chem. Biol.* **2002**, *6*, 243.

(50) Stein, M.; Lubitz, W. *J. Inorg. Biochem.* **2004**, *98*, 862.

(51) Stadler, C.; de Lacey, A. L.; Hernandez, B.; Fernandez, V. M.; Conesa, J. C. *Inorg. Chem.* **2002**, *41*, 4417.

(52) Stadler, C.; de Lacey, A. L.; Montet, Y.; Volbeda, A.; Fontecilla-Camps, J. C.; Conesa, J. C.; Fernandez, V. M. *Inorg. Chem.* **2002**, *41*, 4424.

(53) Bruschi, M.; De Gioia, L.; Zampella, G.; Reiher, M.; Fantucci, P.; Stein, M. *J. Biol. Inorg. Chem.* **2004**, *9*, 873.

(54) Bruschi, M.; Zampella, G.; Fantucci, P.; De Gioia, L. *Coord. Chem. Rev.* **2005**, *249*, 1620.

(55) Kampa, M.; Lubitz, W.; van Gastel, M.; Neese, F. *J. Biol. Inorg. Chem.* **2012**, *17*, 1269.

(56) De Gioia, L.; Fantucci, P.; Guigliarelli, B.; Bertrand, P. *Inorg. Chem.* **1999**, *38*, 2658.

(57) Stein, M.; Lubitz, W. *Phys. Chem. Chem. Phys.* **2001**, *3*, 5115.

(58) Stein, M.; van Lenthe, E.; Baerends, E. J.; Lubitz, W. *J. Am. Chem. Soc.* **2001**, *123*, 5839.

(59) Vignais, P. M.; Billoud, B.; Meyer, J. *FEMS Microbiol. Rev.* **2001**, *25*, 455.

(60) Moura, J. J. G.; Teixeira, M.; Moura, I. *Pure Appl. Chem.* **1989**, *61*, 915.

(61) Lubitz, W.; Reijerse, E.; van Gastel, M. *Chem. Rev.* **2007**, *107*, 4331.

(62) Pandelia, M. E.; Infossi, P.; Stein, M.; Giudici-Orticoni, M. T.; Lubitz, W. *Chem. Commun.* **2012**, *48*, 823.

(63) van der Zwaan, J. W.; Albracht, S. P. J.; Fontijn, R. D.; Slater, E. C. *FEBS Lett.* **1985**, *179*, 271.

(64) Medina, M.; Hatchikian, E. C.; Cammack, R. *Biochim. Biophys. Acta* **1996**, *1275*, 227.

(65) Medina, M.; Williams, R.; Cammack, R.; Hatchikian, E. C. *J. Chem. Soc., Faraday Trans.* **1994**, *90*, 2921.

(66) Fichtner, C.; van Gastel, M.; Lubitz, W. *Phys. Chem. Chem. Phys.* **2003**, *5*, 5507.

(67) Niu, S. Q.; Thomson, L. M.; Hall, M. B. *J. Am. Chem. Soc.* **1999**, *121*, 4000.

(68) Kellers, P.; Pandelia, M.-E.; Currell, L. J.; Goerner, H.; Lubitz, W. *Phys. Chem. Chem. Phys.* **2009**, *11*, 8680.

(69) Bagley, K. A.; Duin, E. C.; Roseboom, W.; Albracht, S. P. J.; Woodruff, W. H. *Biochemistry* **1995**, *34*, 5527.

(70) Pierik, A. J.; Roseboom, W.; Happe, R. P.; Bagley, K. A.; Albracht, S. P. J. *J. Biol. Chem.* **1999**, *274*, 3331.

(71) Schroeder, O.; Bleijlevens, B.; de Jongh, T. E.; Chen, Z.; Li, T.; Fischer, J.; Foerster, J.; Friedrich, C. G.; Bagley, K. A.; Albracht, S. P. J.; Lubitz, W. *J. Biol. Inorg. Chem.* **2007**, *12*, 212.

(72) Neese, F. *Orca, an ab initio, DFT and semiempirical SCF-MO, package 2.8.0 R2327*; University of Bonn: Bonn, Germany, 2011.

(73) Becke, A. D. *Phys. Rev. A* **1988**, *38*, 3098.

(74) Perdew, J. P. *Phys. Rev. B* **1986**, *33*, 8822.

(75) Buehl, M.; Kabrede, H. *J. Chem. Theory Comput.* **2006**, *2*, 1282.

(76) Buehl, M.; Reimann, C.; Pantazis, D. A.; Bredow, T.; Neese, F. *J. Chem. Theory Comput.* **2008**, *4*, 1449.

(77) Weigend, F.; Ahlrichs, R. *Phys. Chem. Chem. Phys.* **2005**, *7*, 3297.

(78) Eichkorn, K.; Weigend, F.; Treutler, O.; Ahlrichs, R. *Theor. Chem. Acc.* **1997**, *97*, 119.

(79) van Lenthe, E.; Snijders, J. G.; Baerends, E. J. *J. Chem. Phys.* **1996**, *105*, 6505.

(80) van Lenthe, E.; van der Avoird, A.; Wormer, P. E. S. *J. Chem. Phys.* **1998**, *108*, 4783.

(81) Klamt, A.; Schuurmann, G. *J. Chem. Soc., Perk. Trans. 2* **1993**, 799.

(82) Grimme, S. *J. Comput. Chem.* **2006**, *27*, 1787.

(83) Soderhjelm, P.; Ryde, U. *J. Mol. Struct.-Theochem* **2006**, *770*, 199.

(84) Jayapal, P.; Sundararajan, M.; Hillier, I. H.; Burton, N. A. *Phys. Chem. Chem. Phys.* **2008**, *10*, 4249.

(85) Bubacco, L.; van Gastel, M.; Groenen, E. J. J.; Vijgenboom, E.; Canters, G. W. *J. Biol. Chem.* **2003**, *278*, 7381.

(86) Neese, F. *J. Chem. Phys.* **2003**, *118*, 3939.

(87) Jonas, V.; Thiel, W. *J. Chem. Phys.* **1995**, *102*, 8474.

(88) Jonas, V.; Thiel, W. *Organometallics* **1998**, *17*, 353.

(89) Barton, B. E.; Rauchfuss, T. B. *J. Am. Chem. Soc.* **2010**, *132*, 14877.

(90) Carroll, M. E.; Barton, B. E.; Gray, D. L.; Mack, A. E.; Rauchfuss, T. B. *Inorg. Chem.* **2011**, *50*, 9554.

(91) Schilter, D.; Nilges, M. J.; Chakrabarti, M.; Lindahl, P. A.; Rauchfuss, T. B.; Stein, M. *Inorg. Chem.* **2012**, *51*, 2338.

(92) Fontecilla-Camps, J. C.; Frey, M.; Garcin, E.; Higuchi, Y.; Nicolet, Y.; Volbeda, A. In *Hydrogen as a fuel*; Cammack, R., Frey, M., Robson, R., Eds.; Taylor & Francis: London, 2001, p 93.

(93) Matias, P. M.; Soares, C. M.; Saraiva, L. M.; Coelho, R.; Morais, J.; Le Gall, J.; Carrondo, M. A. *J. Biol. Inorg. Chem.* **2001**, *6*, 63.

(94) Amara, P.; Volbeda, A.; Fontecilla-Camps, J. C.; Field, M. J. *J. Am. Chem. Soc.* **1999**, *121*, 4468.

(95) Sellmann, D.; Geipel, F.; Moll, M. *Angew. Chem., Int. Ed.* **2000**, *39*, 561.

(96) Goldman, C. M.; Mascharak, P. K. *Comments Inorg. Chem.* **1995**, *18*, 1.

(97) Maroney, M. J.; Bryngelson, P. A. *J. Biol. Inorg. Chem.* **2001**, *6*, 453.

(98) Dole, F.; Fournel, A.; Magro, V.; Hatchikian, E. C.; Bertrand, P.; Guigliarelli, B. *Biochemistry* **1997**, *36*, 7847.

(99) Pipek, J.; Mezey, P. G. *J. Chem. Phys.* **1989**, *90*, 4916.

3925

dx.doi.org/10.1021/ja3115899 | *J. Am. Chem. Soc.* 2013, 135, 3915–3925